

Short-Term Photovoltaic Forecasting Model for Qualifying Uncertainty during Hazy Weather

Xuan Yang^{a,1}, Yunxuan Dong^{a,1}, Lina Yang^a and Thomas Wu^{b,*}

^aSchool of Computer, Electronics and Information, Guangxi University, Nanning, 530004, China

^bSchool of Electrical Engineering, Guangxi University, Nanning, 530004, China

ARTICLE INFO

Keywords:

Photovoltaic forecasting
Entropy
Hierarchical clustering
Attention mechanism

ABSTRACT

Solar energy is one of the most promising renewable energy resources. Forecasting photovoltaic power generation is an important way to increase photovoltaic penetration. However, the difficulty in qualifying uncertainty of PV power generation, especially during hazy weather, makes forecasting challenging. This paper proposes a novel model to address the issue. We introduce a modified entropy to qualify uncertainty during hazy weather while clustering and attention mechanisms are employed to reduce computational costs and enhance forecasting accuracy, respectively. Hyperparameters were adjusted using an optimization algorithm. Experiments on two datasets related to hazy weather demonstrate that our model significantly improves forecasting accuracy compared to existing models.

1. Introduction

Fossil fuels extracted for decades to meet global energy demands, causing serious environmental problems [1]. In contrast, solar power is known for its clean, pollution-free, and sustainable benefits [2]. Fig. 1 shows a significant increase in solar energy capacity over the past decade, with data derived from the International Renewable Energy Agency [3].

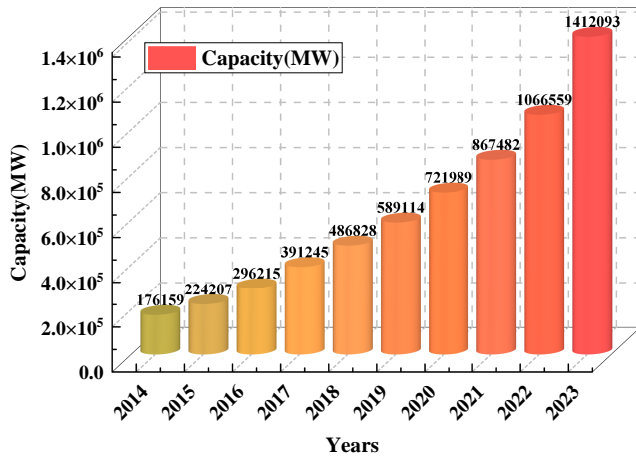


Fig. 1. Global capacity of solar energy from 2014 to 2023.

Photovoltaic (PV) power generation embraces the property of uncertainty due to external factors [4]. Consequently, this uncertainty decreases forecasting accuracy. The power system may lead to serious failures if inaccurate PV forecasting is applied [5]. Consequently, accurate forecasting is essential to improve the stability of the power system [6].

Existing PV forecasting models can be classified into physical, statistical, and hybrid models [7]. Physical models

focus on theoretically explaining the works of PV power systems. Statistical models use data analysis to make forecasts. Hybrid models combine multiple models to improve accuracy. Table 1 lists existing PV forecasting models, showing their descriptions, advantages, and disadvantages.

PV panels receive less solar radiation because sunlight is scattered and particulate matter is deposited on the PV panels during hazy weather [8]. The maintenance of PV panels increases due to the deposition of particles on the panels. The factors create uncertainty in PV power generation and affect power system stability [9]. Therefore, it is essential to qualify uncertainty and make precise forecasts during hazy weather. Visibility drops below 10 kilometres due to light extinction by particulate matter in the atmosphere when the PM_{2.5} concentration reaches or exceeds 100 $\mu\text{g}/\text{m}^3$. The weather can be considered as hazy weather under the circumstances [10]. In this study, we define weather with an air quality level of mild pollution, moderate pollution, or severe pollution as haze.

Existing works consider the impact of haze on PV forecasting [11]. Entropy is a way of qualifying uncertainty in time series [12]. We create modified entropy to qualify uncertainty affected by haze. Then, we use the clustering method based on modified entropy to reduce computational costs. Lastly, we use attention mechanism to make forecasts. Drawing from the analysis above, the main contributions of this work are presented as follows:

- We create the Tsallis Entropy by Weighted Permutation Pattern (TEWPP) to qualify uncertainty during hazy weather. TEWPP examines the distribution of patterns to qualify uncertainty. This method reflects the distribution of PV power generation during hazy weather.
- We use hierarchical clustering based on entropy to reduce the computational costs of the model. This strategy can improve the similarity of elements in

*Corresponding author at School of Electrical Engineering, Guangxi University, Nanning, China.

✉ wuxinzhangcs@outlook.com (T. Wu)

¹These authors contributed to the work equally and should be regarded as co-first authors.

Table 1
Comparison of existing PV forecasting models

Type	Description	Advantages	Disadvantages
Physical models	Simulate the physical process of PV power plants to make forecasts.	Provide high-accuracy forecasts.	Require large computational costs for measuring and updating data.
Statistical models	Build mathematical models with strict assumptions.	Easy to explain the internal mechanisms.	Require input data to conform to the assumptions.
Machine models	Make forecasts based on a huge amount of historical data.	Handle complex nonlinear relationships.	Difficult to explain the internal mechanisms.
Hybrid models	Combine multiple models according to the characteristics of forecasting models to improve accuracy and reliability.	Overcome limitations of a single model, improving accuracy and reliability.	Result in higher computational costs than a single model.

the same cluster, thereby reducing the computational costs.

- We use modified Retention Network (RetNet) to extract the features and make forecasts. CNN uses kernel on input data to extract local features through multiplication and summation. RetNet is used to make forecasts. The model improves the forecasting accuracy.
- We adopt the Non-dominated Sorting Genetic Algorithm-II (NSGA-II) to optimize the hyperparameters. NSGA-II searches for optimal solutions by simulating natural selection and genetic mechanisms. The robustness of the model can be enhanced by using NSGA-II.
- We use datasets from a PV power station in a specific region of Jiangsu, China and another from Beijing, China. The experimental results are evaluated through evaluation metrics, and these results are compared to others obtained from traditional models.

The remainder of this paper is organized as follows. Section 2 presents an overview of related works. Section 3 introduces the optimal goal of the system model. Section 4 gives an architecture and a detailed description of CCRetNet. Section 5 provides an overview of the experimental setup, air quality analysis, and the results of single-step and multi-step forecasting experiments in Jiangsu Province and Beijing. Section 6 provides conclusions.

2. Related works

PV forecasting is crucial for power systems [13]. Hence, scholar made most efforts in this regard [14], [7], [15], [16]. In this section, we review related works from two aspects: weather factors and models.

Weather factors, particularly haze, are taken into account in the field of PV forecasting [17]. Yao et al. [18] introduced the air quality index and used the support vector machine algorithm to develop a new model for estimating solar radiation under haze conditions. The model improved

accuracy and was suitable for regions with limited equipment or high pollution but did not explore using other neural network algorithms to assess the coupling effects of haze and weather parameters. Fan et al. [19] employed a support vector machine model to improve global and diffuse solar radiation predictions by incorporating air quality index and various pollutants. The approach significantly enhanced accuracy, particularly in heavily polluted areas. However, as the number of input pollutants increases, the complexity and computational resource consumption also rise, with diminishing returns on improvement. The research developed a new daily diffuse solar radiation model by incorporating the air quality index to improve accuracy in smog-affected areas [20]. The air quality index adjustment significantly enhanced accuracy, especially in polluted regions like Beijing. However, the model's effectiveness varied across different regions, requiring further optimization for broader applicability.

Nowadays, the attention mechanism is used in the field of PV forecasting [21]. The research used improved complementary empirical mode decomposition and variational mode decomposition for reducing noise [2]. The attention mechanism focused on critical information to improve accuracy. The model was adjusted to data features to improve accuracy, whereas the complexity of the model limited its application. Yu et al. [13] used temporal, frequency, and fourier attention to capture detailed time-series insights from PV power data. The attention mechanism focused on crucial temporal and environmental features, thereby enhancing accuracy. However, this approach also obscured the significance of the time series itself. Wang et al. [22] combined a temporal convolutional network with an improved deep residual shrinkage network. The special attention mechanism in the model enhanced the ability to extract features in noisy environments. However, the model required significant computational resources.

Table 2 summarizes other related works, including details of works, advantages, and disadvantages, where "Ref." denotes "References".

Table 2

List of related works

PV forecasting considering weather factors				
Ref.	Year	Details	Advantages	Disadvantages
[11]	2021	Photovoltaic power; Power forecasting; Hazy conditions; Artificial neural network	Enhanced accuracy in polluted environments.	Relied on accuracy of air quality index data.
[23]	2020	Air pollution; Prediction; Solar radiation	Improved accuracy with the bat algorithm, enhancing convergence speed.	Resulted in larger computation under different pollution levels.
PV forecasting compared model				
Ref.	Year	Details	Advantages	Disadvantages
[24]	2023	Photovoltaic power forecast; Channel attention mechanism; Time series forecasting	Improved accuracy. Available for multivariate time series forecasting.	Caused a risk of overfitting.
[25]	2023	Solar photovoltaic power; Short-term prediction; Deep learning; Attention net	Enhanced processing capabilities through attention mechanisms.	Sensitive to quality of input data.
[26]	2023	Temporal convolutional attention neural networks; PV power forecasting	Captured the spatio-temporal features and improved the accuracy.	Only represented the ultra-short-term prediction.

Table 3

List of abbreviations and parameters

Abbreviations	Description	Abbreviations	Description
MSR	Multi-Scale Retention	PV	Photovoltaic
CCRetNet	Clustering and CNN-RetNet	Ref.	Reference
CNN	Convolutional Neural Network	RetNet	Retention Network
FLOPs	Floating Point Operations	RMSE	Root Mean Squared Error
FFN	Feed-Forward Network	RNN	Recurrent Neural Network
GRU	Gate Recurrent Unit	RS	Random Search
LSTM	Long Short Term Memory	TPE	Tree-structured Parzen Estimator
MAE	Mean Absolute Error	TEWPP	The Tsallis Entropy by Weighted Permutation Pattern
Parameter	Description	Parameter	Description
k	The optimal number of PV power generation clusters	β	The parameter for TEWPP
$\mathcal{L}_n(\cdot)$	The loss function for the n -th cluster	$\mathbf{x}_p, \mathbf{x}_q$	The series of PV power generation
ϕ_n	The parameters for the n -th model	\mathbf{w}	The weight between the \mathbf{x}_p and \mathbf{x}_q
ψ_n	The hyperparameters for the n -th model	$\mathbf{x}_p(n), \mathbf{x}_q(n)$	The element of \mathbf{x}_p and \mathbf{x}_q , respectively
Φ	The set of all model parameters	$d(\cdot, \cdot)$	The distance
Ψ	The set of all model hyperparameters	d_n	Abbreviation for $d(\mathbf{x}_p(n), \mathbf{x}_q(n))$
ϕ_n^*	The optimal parameters for the n -th model in training phase	d'_n	Sorted d_n
ψ_n^*	The optimal hyperparameters for the n -th model in validating phase	C_p	The p -th cluster
α	The weight parameter for training phase and validating phase	d	Hidden dimension for RetNet
\mathbf{x}	The series of PV power generation	\mathbf{X}^0, \mathbf{X}	The input data for RetNet
T	The length of series for PV power generation \mathbf{x}, \mathbf{x}_p and \mathbf{x}_q	$\mathbf{W}_V, \mathbf{W}_Q, \mathbf{W}_K$	The weight matrices
$\mathbf{x}_i^{m,\tau}$	The segments of \mathbf{x}	$\mathbf{V}, \mathbf{Q}, \mathbf{K}$	The projection
m	The dimension of $\mathbf{x}_i^{m,\tau}$	$\mathbf{v}_n, \mathbf{q}_n, \mathbf{k}_n$	The projection
τ	The time lag of $\mathbf{x}_i^{m,\tau}$	s_n	The state
$\pi_j^{m,\tau}$	The unique permutation	\mathbf{o}_n	Vectors \mathbf{v}_n mapped through state s_n
ω_t	The weight parameter of $\mathbf{x}_i^{m,\tau}$	γ	Attenuation factor
$\mathbb{I}_A(\cdot)$	The indicator function of set A	h	The number of retention heads in each layer
$\hat{\pi}(\mathbf{x})$	The permutation of the series \mathbf{x}	d_h	The head dimension

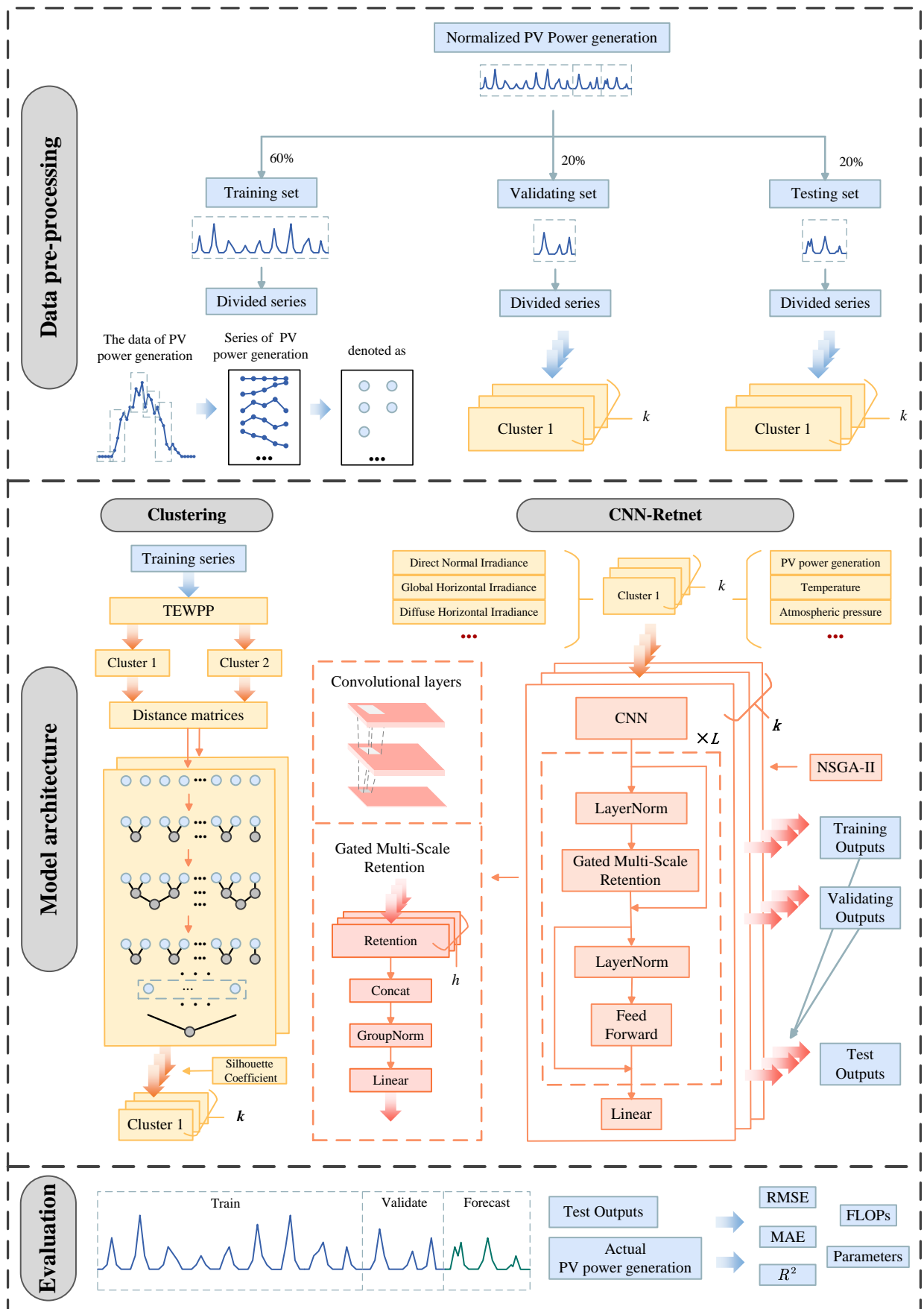


Fig. 2. Framework of proposed model

3. Problem definition

Let k represent the optimal number of clusters for PV power generation. $\mathcal{L}_n(\cdot)$ denotes the loss function of the forecasting model for the n -th cluster. The set of parameters is denoted by ϕ_n , and the set of hyperparameters is denoted by ψ_n for the n -th model. $\Phi = \{\phi_1, \phi_2, \dots, \phi_k\}$ denotes the set of parameters for all model and $\Psi = \{\psi_1, \psi_2, \dots, \psi_k\}$ denotes the set of hyperparameters for all model.

During the training phase, the objective is to minimize the loss function for each cluster. The objective function denotes as follows:

$$\min_{\Phi} \sum_{n=1}^k \mathcal{L}_n(\phi_n). \quad (1)$$

The optimal set ϕ_n^* is determined during the training phase when equation (1) obtains its minimum value (i.e., $\phi_n^* = \arg \min_{\Phi} \sum_{n=1}^k \mathcal{L}_n(\phi_n)$).

For the validating phase, it should be assigned to the cluster that minimizes the loss function for the new data segment denoted by \mathbf{x} . The objective function denotes as follows:

$$\min_{n \in \{1, \dots, k\}} \mathcal{L}_n(\mathbf{x}, \psi_n; \phi_n^*). \quad (2)$$

The optimal set ψ_n^* is determined during the validating phase when equation (2) obtains its minimum value (i.e., $\psi_n^* = \arg \min_{\Psi} \sum_{n=1}^k \mathcal{L}_n(\psi_n)$).

Combining both phases, the problem is defined as follows:

$$\min \left(\alpha \sum_{n=1}^k \mathcal{L}_n(\phi_n) + (1 - \alpha) \sum_{n=1}^k \mathcal{L}_n(\mathbf{x}, \psi_n; \phi_n^*) \right), \quad (3)$$

where α denotes a weighting parameter that balances minimizing the training loss and the validating loss.

Equation (3) ensures that the model of each cluster is well-trained (i.e., minimizing the loss function during training) and that new data is assigned to the most suitable cluster (i.e., minimizing the loss function during validating).

4. Proposed model

4.1. Model architecture

In this paper, we propose CCRetNet based on two crucial components: Clustering and CNN-RetNet. The architecture of the proposed model is demonstrated in Fig. 2. In brief, the aim of the proposed model is to qualify uncertainty, extract features, and improve forecasting accuracy during hazy weather.

We create the Tsallis Entropy by Weighted Permutation Pattern (TEWPP) to qualify uncertainty. Based on TEWPP, hierarchical clustering is used to reduce the computational costs. The hierarchical clustering utilizes the novel calculation of distance between series and the median linkage criterion as referenced in [27]. Additionally, we use modified RetNet to extract the features and make forecasts. CNN extracts the features, and RetNet is used to make forecasts. NSGA-II optimizes the hyperparameters to enhance the robustness.

4.2. Clustering method

This section covers both TEWPP and hierarchical clustering. We first introduce TEWPP following the model architecture.

4.2.1. The tsallis entropy by weighted permutation pattern

The weighted permutation pattern is a method for time series analysis. Compared to permutation patterns, it better captures complex structures [28].

Considering a PV power generation series $\mathbf{x} = \{\mathbf{x}(1), \mathbf{x}(2), \dots, \mathbf{x}(T)\}$ with length T , we obtain its segment $\mathbf{x}_t^{m,\tau} = \{\mathbf{x}(t), \mathbf{x}(t + \tau), \dots, \mathbf{x}(t + (m - 1)\tau)\}$ for $t = 1, 2, \dots$, where m and τ respectively represent the dimension and time lag. Every $\mathbf{x}_t^{m,\tau}$ has $m!$ possible permutations, and it results in a unique permutation $\pi_j^{m,\tau}$.

Before defining the probability of the weighted permutation pattern $p_{\omega}(\pi_j^{m,\tau})$, we first define $\bar{\mathbf{x}}_t^{m,\tau}$ and the weight value ω_t .

$\bar{\mathbf{x}}_t^{m,\tau}$ is the arithmetic mean of $\mathbf{x}_t^{m,\tau}$. For every $\mathbf{x}_t^{m,\tau}$, the weight value ω_t is defined as follows:

$$\omega_t = \frac{1}{m} \sum_{k=1}^m [\mathbf{x}(t + (k - 1)\tau) - \bar{\mathbf{x}}_t^{m,\tau}]^2. \quad (4)$$

The probability of the weighted permutation pattern is defined as follows [29]:

$$p_{\omega}(\pi_j^{m,\tau}) = \frac{\sum_{t \leq T - (m-1)} \mathbb{I}_{u:\hat{\pi}(u)=\pi_j}(\mathbf{x}_t^{m,\tau}) \omega_t}{\sum_{t \leq T - (m-1)} \omega_t}, \quad (5)$$

where $\mathbb{I}_A(\mathbf{x})$ denotes the indicator function of set A defined as $\mathbb{I}_A(\mathbf{x}) = 1$ if $\mathbf{x} \in A$ and $\mathbb{I}_A(\mathbf{x}) = 0$ if $\mathbf{x} \notin A$. $\hat{\pi}(\mathbf{x})$ is a permutation of the series \mathbf{x} .

We create TEWPP by applying the weighted permutation pattern to Tsallis entropy inspired by [30]. The calculation of TEWPP is defined as follows:

$$H_{\beta}(\mathbf{x}, m, \tau) = \frac{1}{\beta - 1} \left[1 - \sum_{j=1}^{m!} (p_{\omega}(\pi_j^{m,\tau}))^{\beta} \right], \quad (6)$$

$\beta > 0, \beta \neq 1,$

where β is the parameter. $H_{\beta}(\mathbf{x}, m, \tau)$ reduce to Shannon entropy when $\beta \rightarrow 1$. $H_{\beta}(\mathbf{x}, m, \tau)$ is influenced by large probability events when the parameter was set to $\beta > 1$. $H_{\beta}(\mathbf{x}, m, \tau)$ is influenced by small probability events when the parameter was set to $\beta < 1$.

Based on TEWPP, we categorize the PV power series into clusters of large uncertainty and small uncertainty. Hierarchical clustering is used for the clusters of large uncertainty and small uncertainty, respectively.

4.2.2. Hierarchical clustering

The core of hierarchical clustering is to construct a structure based on the distance between series and the distance between clusters. Consequently, different distance measures can result in different clustering outcomes. We

will next present the calculations for the distance between series (equation (10)) and between clusters (equation (11)), followed by the hierarchical clustering process (algorithm 1) and the evaluation metric (equation (14)).

Let $\mathbf{x}_p = \{\mathbf{x}_p(t)\}^T$ and $\mathbf{x}_q = \{\mathbf{x}_q(t)\}^T$ are series of PV power generation with T-dimension for $p \neq q$. The weight $\mathbf{w} = \{w_n\}^T$ between the \mathbf{x}_p and \mathbf{x}_q is defined as below:

$$\mathbf{w} = \{w_n \mid w_n = \max\left\{\frac{\mathbf{x}_p(n)}{(\sum_{m_1=1}^T \mathbf{x}_p(m_1))}, \frac{\mathbf{x}_q(n)}{(\sum_{m_2=1}^T \mathbf{x}_q(m_2))}\right\}, n = 1, 2, \dots, T\}. \quad (7)$$

The distance $d(\mathbf{x}_p(n), \mathbf{x}_q(n))$ between $\mathbf{x}_p(n)$ and $\mathbf{x}_q(n)$ is defined as follows:

$$d(\mathbf{x}_p(n), \mathbf{x}_q(n)) = w_n(\mathbf{x}_p(n) - \mathbf{x}_q(n))^2. \quad (8)$$

For convenience, we write $d(\mathbf{x}_p(n), \mathbf{x}_q(n))$ as d_n . We sort the $\{d_n\}^T$ from largest to smallest to get the $\{d'_n\}^T$. Therefore d'_n satisfies :

$$d'_1 \geq d'_2 \geq \dots \geq d'_T. \quad (9)$$

We define the calculation for the distance between series. The calculation adopts the average of the $\{d'_n\}^T$ in the middle, thereby reducing the influence of extreme values. Hence, the distance between \mathbf{x}_p and \mathbf{x}_q is defined as follows:

$$d(\mathbf{x}_p, \mathbf{x}_q) = \frac{1}{n_{Q_3} - n_{Q_2} + 1} \sum_{n=n_{Q_2}}^{n_{Q_3}} d'_n, \quad (10)$$

where the position index of the second quartile Q_2 and the third quartile Q_3 denote n_{Q_2} and n_{Q_3} , respectively.

Traditional distance calculations between clusters in hierarchical clustering include the single linkage criterion, complete linkage criterion, average linkage criterion, and median linkage criterion. We use a novel linkage criterion as referenced in [27] to compute the distance between different clusters as follows:

$$d_{\alpha_1, \alpha_2}(C_p, C_q) = \frac{1}{|S_{\alpha_1(N), \alpha_2(N)}|} \sum_{(\mathbf{x}_p, \mathbf{x}_q) \in S_{\alpha_1(N), \alpha_2(N)}} d(\mathbf{x}_p, \mathbf{x}_q), \quad (11)$$

where $S_{\alpha_1(N), \alpha_2(N)}$ is a subset of all possible pairs $(\mathbf{x}_p, \mathbf{x}_q)$, $\mathbf{x}_p \in C_p, \mathbf{x}_q \in C_q$. We define $S_{\alpha_1(N), \alpha_2(N)}$ as follows:

$$S_{\alpha_1(N), \alpha_2(N)} = \{(\mathbf{x}_p, \mathbf{x}_q), \mathbf{x}_p \in C_p, \mathbf{x}_q \in C_q \mid r_{(\alpha_1(N))} \leq d(\mathbf{x}_p, \mathbf{x}_q) \leq r_{(\alpha_2(N))}\}, \quad (12)$$

where C_p and C_q stand for different clusters. $N = |C_p| + |C_q|$, where $|C_p|$ means the number of elements in cluster C_p . $r_{(1)} \leq r_{(2)} \leq \dots \leq r_{(N)}$ denotes a rank-ordered set of the distances $d(\mathbf{x}_p, \mathbf{x}_q)$. Obviously, $r_{(1)}$ and $r_{(N)}$ represent the minimum distance and the maximum distance, respectively. To more effectively group similar segments while minimizing the impact of extreme values of the segments, the parameter $\alpha_1(N)$ and $\alpha_2(N)$ are set to $N/2$ and $3N/4$ (i.e. $r_{\alpha_1(N)}$ and $r_{\alpha_2(N)}$ represent the second quartile Q_2 and the third quartile Q_3 of the distances $d(\mathbf{x}_p, \mathbf{x}_q)$ respectively).

Algorithm 1 Hierarchical clustering algorithm

Input: Series \mathcal{X} , distance matrix \mathcal{D} between series, linkage criterion

Output: A set of clusters and a dendrogram representing the hierarchy of clusters

- 1: Initialize each series as a single cluster
 - 2: **while** number of clusters > 1 **do**
 - 3: Calculate the distance between all pairs of clusters using the specified \mathcal{D}
 - 4: Merge the two closest clusters based on the linkage criterion
 - 5: Update the distance matrix based on the linkage criterion
 - 6: **end while**
 - 7: Construct the dendrogram based on the merge history
 - 8: **return** Clusters and dendrogram
-

We use hierarchical clustering according to the definitions of the above two distant calculations. The process of hierarchical clustering is detailed in algorithm 1.

We employ the silhouette coefficient [31] to determine the most suitable number of clusters. The silhouette coefficient is a way to evaluate the clustering effect by combining cohesion and separation. The value spans from -1 to 1 . The closer silhouette coefficient of \mathbf{x}_p is to 1 , the more compact \mathbf{x}_p is within its cluster.

Let $a(\mathbf{x}_p)$ denotes the cohesion of the cluster C_p and $b(\mathbf{x}_p)$ denotes the separation between clusters. $a(\mathbf{x}_p)$ is defined as mean distance from the segment \mathbf{x}_p to all other segments in the same cluster. $b(\mathbf{x}_p)$ denotes smallest mean distance from the segment \mathbf{x}_p all segments in any other cluster. The calculations of $a(\mathbf{x}_p)$ and $b(\mathbf{x}_p)$ are defined as follows:

$$a(\mathbf{x}_p) = \frac{1}{|C_p| - 1} \sum_{\mathbf{x}_{p_1} \in C_p, p \neq p_1} d(\mathbf{x}_p, \mathbf{x}_{p_1}),$$

$$b(\mathbf{x}_p) = \min_{C_p \neq C_q} \frac{1}{|C_q|} \sum_{\mathbf{x}_q \in C_q} d(\mathbf{x}_p, \mathbf{x}_q). \quad (13)$$

The silhouette coefficient $S(\mathbf{x}_p)$ for $\forall \mathbf{x}_p$ is calculated as follows:

$$S(\mathbf{x}_p) = \frac{b(\mathbf{x}_p) - a(\mathbf{x}_p)}{\max\{a(\mathbf{x}_p), b(\mathbf{x}_p)\}}. \quad (14)$$

The average of the silhouette coefficient for the entire dataset is calculated as follows:

$$S = \frac{1}{|\Omega_k|} \sum_{\mathbf{x}_p \in \Omega_k} S(\mathbf{x}_p), \quad (15)$$

where Ω_k represents the set of all the segments.

4.3. CNN-RetNet

In this section, we use CNN-RetNet to make forecasts inspired by [32].

4.3.1. CNN

To extract features from PV power generation data, we add three convolutional layers before applying RetNet. The first convolutional layer maps the input data. The second layer extracts initial features, while the third layer captures higher-order features.

4.3.2. Retention

Given input data $X^0 \in \mathbb{R}^{l_x \times d}$ denoted X (i.e. $X = \{\mathbf{x}_n\}^{l_x}$ and $\mathbf{x}_n \in \mathbb{R}^{1 \times d}$), where d denotes hidden dimension. Let the weight define $\mathbf{W}_V \in \mathbb{R}^{d \times d}$. We project it to a one-dimensional function as follows:

$$\mathbf{v}_n = \mathbf{x}_n \cdot \mathbf{W}_V, \quad (16)$$

where vector $\mathbf{v}_n \in \mathbb{R}^{1 \times d}$. $\mathbf{W}_Q, \mathbf{W}_K \in \mathbb{R}^{d \times d}$ denote the weights that need to be learned. Similarly, the projections of \mathbf{Q}, \mathbf{K} , \mathbf{q}_n and \mathbf{k}_n are defined as follows:

$$\mathbf{Q} = \mathbf{X}\mathbf{W}_Q, \mathbf{K} = \mathbf{X}\mathbf{W}_K, \quad (17)$$

$$\mathbf{q}_n = \mathbf{x}_n \cdot \mathbf{W}_Q \in \mathbb{R}^{1 \times d}, \mathbf{k}_n = \mathbf{x}_n \cdot \mathbf{W}_K \in \mathbb{R}^{1 \times d}. \quad (18)$$

Consider \mathbf{o}_n is mapped to a vector \mathbf{v}_n by state $s_n \in \mathbb{R}^{d \times d}$. The state s_n and the vector \mathbf{o}_n are defined as follows:

$$\begin{aligned} s_n &= \mathbf{B}s_{n-1} + \mathbf{k}_n^T \mathbf{v}_n, \\ \mathbf{o}_n &= \mathbf{q}_n s_n = \sum_{s=1}^n \mathbf{q}_n \mathbf{B}^{n-s} \mathbf{k}_s^T \mathbf{v}_s, \end{aligned} \quad (19)$$

where $\mathbf{B} \in \mathbb{R}^{d \times d}$ denotes a diagonal matrix, defined as $\mathbf{B} = \Lambda(\gamma e^{i\theta})\Lambda^{-1}$. With the equation (18), equation (19) and the definition of Λ , we can rewrite the expression of \mathbf{o}_n as follows:

$$\begin{aligned} \mathbf{o}_n &= \sum_{s=1}^n \mathbf{q}_n (\gamma e^{i\theta})^{n-s} \mathbf{k}_s^T \mathbf{v}_s \\ &= \sum_{s=1}^n (\mathbf{q}_n (\gamma e^{i\theta})^n) (\mathbf{k}_s (\gamma e^{i\theta})^{-s})^T \mathbf{v}_s, \end{aligned} \quad (20)$$

where $\mathbf{q}_n (\gamma e^{i\theta})^n$, $\mathbf{k}_s (\gamma e^{i\theta})^{-s}$ are relative position embeddings proposed by Transformer [33]. Additionally, when γ is a scalar, equation (20) can be further simplified as follows:

$$\mathbf{o}_n = \sum_{s=1}^n \gamma^{n-s} (\mathbf{q}_n e^{in\theta}) (\mathbf{k}_s e^{-is\theta})^\dagger \mathbf{v}_s, \quad (21)$$

where \dagger is the conjugate transpose.

a. The parallel representation

The equation (23) represents the parallel of retention.

$$\mathbf{Q} = (\mathbf{X}\mathbf{W}_Q) \odot \Theta, \mathbf{K} = (\mathbf{X}\mathbf{W}_K) \odot \bar{\Theta}, \mathbf{V} = \mathbf{X}\mathbf{W}_V, \quad (22)$$

$$\Theta_n = e^{in\theta}, \quad D_{ns} = \begin{cases} \gamma^{n-s}, & n \geq s \\ 0, & n < s \end{cases}$$

$$\text{Retention}(\mathbf{X}, \gamma) = (\mathbf{Q}\mathbf{K}^T \odot \mathbf{D})\mathbf{V}, \quad (23)$$

where \odot denotes the two matrices are multiplied element by element. $\Theta = \{\theta_n\}^{l_x}$ and $\bar{\Theta}$ denotes the complex conjugate of Θ .

b. The recurrent representation of retention

The equation (24) represents the recurrent of retention.

$$\begin{aligned} \mathbf{S}_n &= \gamma \mathbf{S}_{n-1} + \mathbf{k}_n^T \mathbf{v}_n, \\ \text{Retention}(\mathbf{x}_n, \gamma) &= \mathbf{q}_n \mathbf{S}_n, \quad n = 1, \dots, l_x, \end{aligned} \quad (24)$$

where the definition of \mathbf{S}_n is similar to the state s_n . \mathbf{q}_n , \mathbf{k}_n and \mathbf{v}_n can be derived from equation (22).

c. The chunkwise recurrent representation of retention

We divide the input into chunks and apply the parallel representation specified in equation (23) for computations within each chunk. In contrast, cross-chunk information is handled using the recurrent representation described in equation (24). Here, b represents the chunk length. The retention output for the i -th chunk is calculated as follows:

$$\begin{aligned} \mathbf{Q}_{[i]} &= \mathbf{Q}_{bi:b(i+1)}, \mathbf{K}_{[i]} = \mathbf{K}_{bi:b(i+1)}, \mathbf{V}_{[i]} = \mathbf{V}_{bi:b(i+1)}, \\ \mathbf{R}_i &= \mathbf{K}_{[i]}^T (\mathbf{V}_{[i]} \odot \zeta) + \gamma^b \mathbf{R}_{i-1}, \zeta_i = \gamma^{b-i-1}, \\ \text{Retention}(\mathbf{X}_{[i]}, \gamma) &= \underbrace{(\mathbf{Q}_{[i]} \mathbf{K}_{[i]}^T \odot \mathbf{D}) \mathbf{V}_{[i]}}_{\text{Inner-Chunk}} + \underbrace{(\mathbf{Q}_{[i]} \mathbf{R}_{i-1}) \odot \xi}_{\text{Cross-Chunk}}, \\ \xi_i &= \gamma^{i+1}, \end{aligned} \quad (25)$$

where the definition of \mathbf{R}_i is similar to the state s_n . The three forms of retention correspond to a, b, and c in figure 3 respectively.

4.3.3. Gated multi-scale retention

h retention heads are employed in each layer, and d_h satisfies $h = d/d_h$, where d_h denotes head dimension. Each heads operates on distinct parameter matrices $\mathbf{W}_Q, \mathbf{W}_K, \mathbf{W}_V \in \mathbb{R}^{d \times d}$ and γ . The output of the MSR layer for the input \mathbf{X} is defined as follows:

$$\gamma = 1 - 2^{-5-\text{arange}(0,h)} \in \mathbb{R}^h,$$

$$\text{head}_i = \text{Retention}(\mathbf{X}, \gamma_i),$$

$$\mathbf{Y} = \text{GroupNorm}_h(\text{Concat}(\text{head}_1, \dots, \text{head}_h)),$$

$$\text{MSR}(\mathbf{X}) = (\text{swish}(\mathbf{X}\mathbf{W}_G) \odot \mathbf{Y})\mathbf{W}_O, \quad (26)$$

where $\mathbf{W}_G, \mathbf{W}_O \in \mathbb{R}^{d \times d}$ are learnable parameters. Swish is the activation function. Since there is a different γ for each head, the output of each head needs to be normalized separately and then combined.

4.3.4. Retention network

In an L -layer Retention Network, we integrate multi-scale retention (MSR) with the feed-forward network (FFN). Let W_1 and W_2 be parameters. FFN is calculated as follows:

$$\text{FFN}(\mathbf{X}) = \text{gelu}(\mathbf{X}\mathbf{W}_1)\mathbf{W}_2, \quad (27)$$

where gelu denotes the activation function.

The calculation for the l -th layer of RetNet is denoted as follows:

$$\mathbf{Y}^l = \text{MSR}(\text{LayerNorm}(\mathbf{X}^l)) + \mathbf{X}^l \quad (28)$$

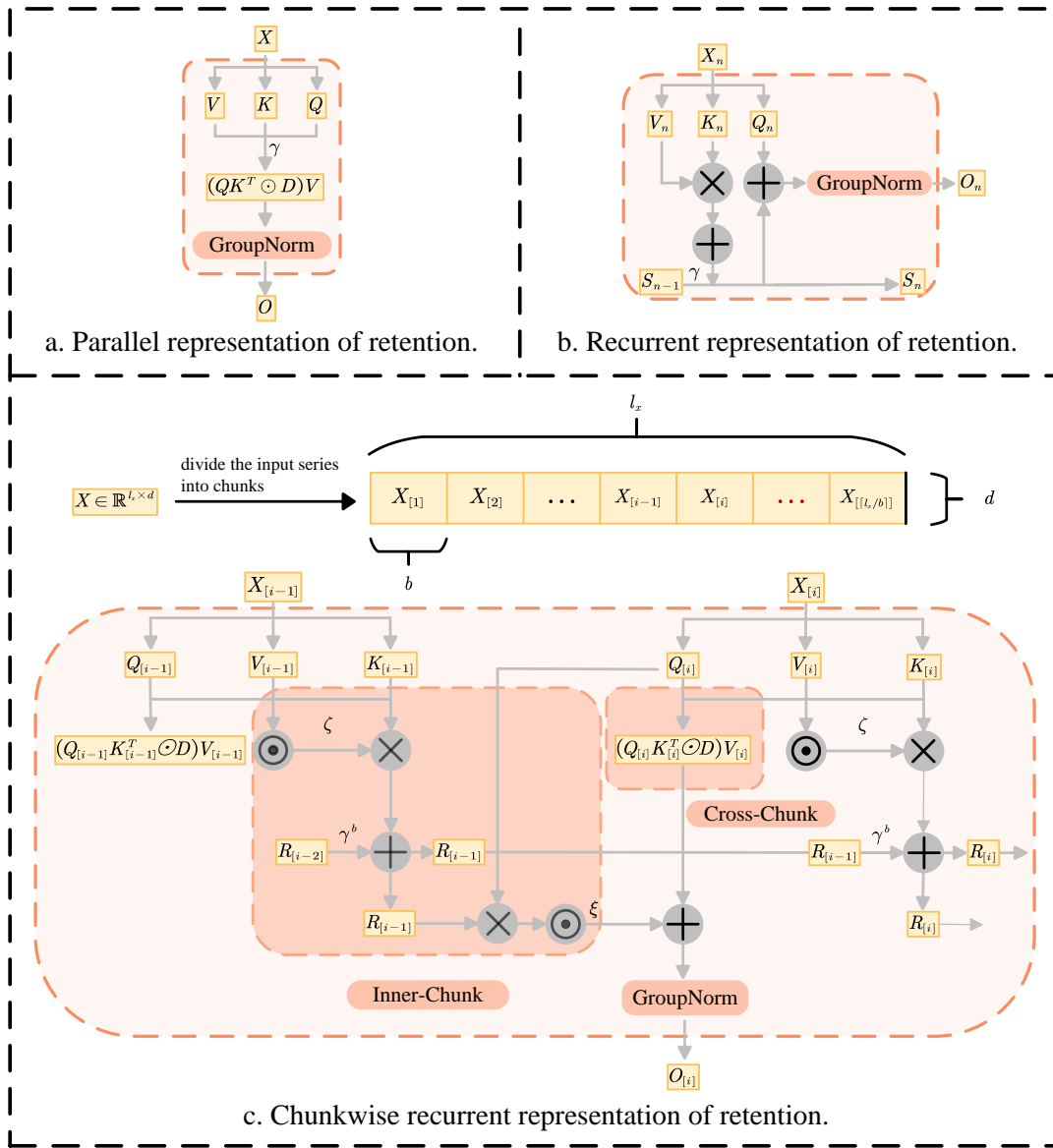


Fig. 3. Three forms of retention

$$X^{l+1} = \text{FFN}(\text{LayerNorm}(Y^l)) + Y^l \quad (29)$$

where $l \in [0, L]$. The output denotes X^L . The process of RetNet is shown in algorithm 2.

4.4. Optimization

NSGA-II is used in multi-objective optimization and is known for finding a balanced set of solutions. It is commonly applied in engineering, economics, logistics, and other fields. In this study, we utilize the NSGA-II algorithm.

Algorithm 2 RetNet Algorithm

Input: The input data X .

Output: The PV power generation data.

- 1: **for** each layer $l = 1$ to L **do**
 - 2: **for** each head $i = 1$ to h **do**
 - 3: $\text{head}_i \leftarrow \text{Retention}(X, \gamma_i)$
 - 4: **end for**
 - 5: $Y \leftarrow \text{GroupNorm}_h(\text{Concat}(\text{head}_1, \dots, \text{head}_h))$
 - 6: $\text{MSR}(X) \leftarrow (\text{swish}(XW_G) \odot Y)W_O$
 - 7: $Y^l \leftarrow \text{MSR}(\text{LayerNorm}(X^l)) + X^l$
 - 8: $X^l \leftarrow \text{FFN}(\text{LayerNorm}(Y^l)) + Y^l$
 - 9: **end for**
 - 10: Output $\leftarrow X_L$
-

Table 4

Statistical table of PV power generation and meteorological variables in a specific region of Jiangsu Province, 2015

Variable Name	Unit	Max Value	Min Value	Mean Value
Direct Normal Irradiance	W/m ²	1051.68	0.00	210.40
Global Horizontal Irradiance	W/m ²	962.29	0.00	192.52
Diffuse Horizontal Irradiance	W/m ²	94.65	0.00	18.94
Temperature of Component	°C	53.00	-6.30	16.65
Ambient Temperature	°C	36.50	-4.70	15.44
Atmospheric Pressure	hPa	1040.40	994.00	1017.52
Relative Humidity	%	100.00	15.00	76.82
PV Power Generation	MW	115.775	-0.44	17.68

Table 5

Statistical table of PV power generation and meteorological variables in Beijing, 2019

Variable Name	Unit	Max Value	Min Value	Mean Value
Air Temperature	°C	40.973	-16.618	12.922
Precipitation	mm/hour	7.493	0.000	0.056
Snowfall	mm/hour	3.242	0.000	0.002
Snow Mass	kg/m ²	7.001	0.000	0.148
Air Density	kg/m ³	1.378	1.093	1.212
Ground-level Solar Irradiance	W/m ²	1012.688	0.000	191.877
Top of Atmosphere Solar Irradiance	W/m ²	1259.022	0.000	328.785
Cloud Cover Fraction	[0, 1]	0.999	0.000	0.351
PV Power Generation	MW	0.875	0.000	0.177

5. Experiments

5.1. Experimental setup

5.1.1. Datasets

Both datasets are multi-sample, multivariate, and exhibit temporal variation. One dataset, which contains eight variables, originates from a 2015 PV power station in a specific region of Jiangsu Province, China. The other dataset originates from Beijing, China, collected in 2019 and contains nine variables. Table 4 details the variables in the 2015 Jiangsu dataset, while Table 5 outlines the variables in the 2019 Beijing dataset.

5.1.2. Implementation details

We apply min-max normalization to each variable at different scales. The model generates outputs from normalized input data, and outputs are inversely normalized for evaluation.

In calculating TEWPP, we set $m = 5$, $\tau = 2$, and $\beta = 0.8$. We employ the silhouette coefficient to determine the optimal number of clusters. The detailed introduction of the silhouette coefficient has already been explained in Section 4.2.2. The hyperparameters are adjusted using the Optuna optimal framework.

5.1.3. Evaluation metrics

The objective of PV forecasting is to improve accuracy while reducing computational costs. Consequently, we use

three evaluation metrics for accuracy and two for computational costs.

There are three evaluation metrics for accuracy: the Root Mean Squared Error (RMSE), the Mean Absolute Error (MAE), and the coefficient of determination R^2 . Each of them offers a unique perspective. RMSE focuses on larger values, MAE focuses on median error, and Coefficient of determination R^2 focuses on the proportion of variance in the dependent variable forecasting from the independent variables. The calculations of metrics are as follows:

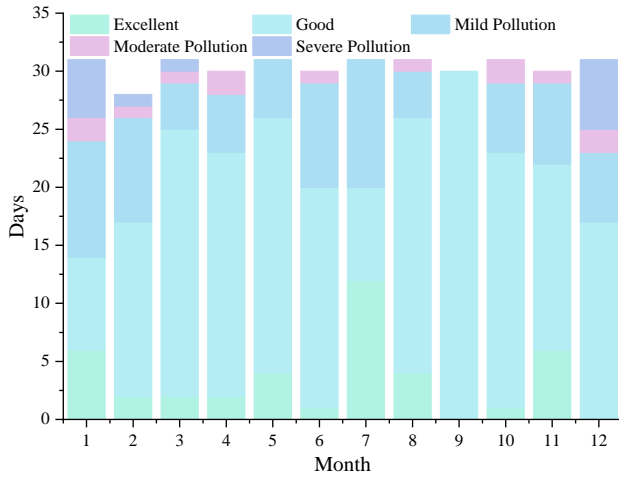
$$\text{RMSE} = \left(\frac{1}{M} \sum_{i=1}^M (y_i - \hat{y}_i)^2 \right)^{\frac{1}{2}}, \quad (30)$$

$$\text{MAE} = \frac{1}{M} \sum_{i=1}^M |y_i - \hat{y}_i|, \quad (31)$$

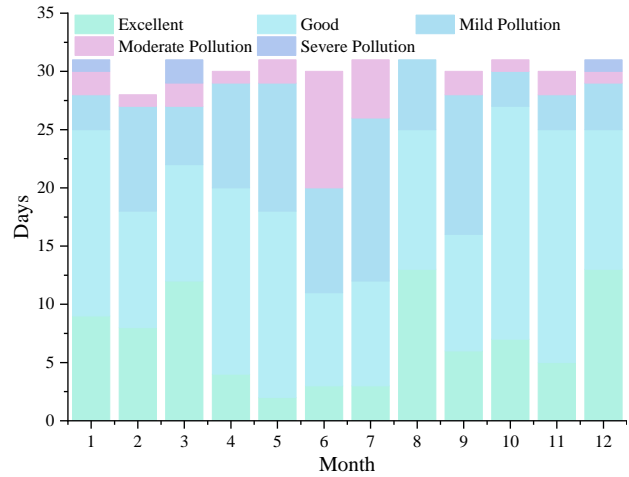
$$R^2 = 1 - \frac{\sum_{i=1}^M (y_i - \hat{y}_i)^2}{\sum_{i=1}^M (y_i - \bar{y})^2}, \quad (32)$$

where y_i denotes the actual value, \hat{y}_i denotes the forecasting value. \bar{y} denotes the mean of the actual values. M denotes the number of samples.

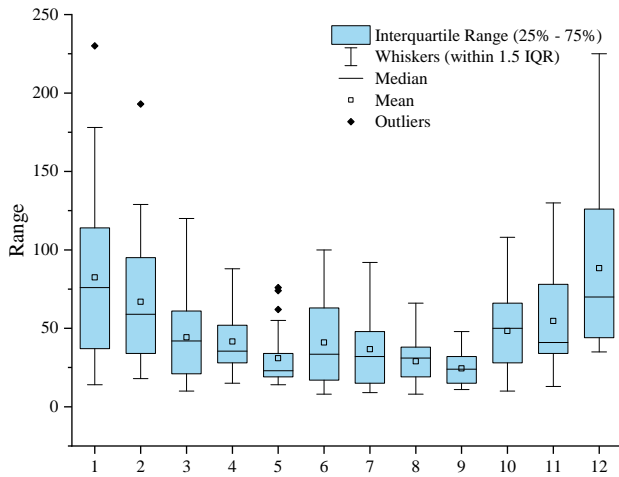
There are two evaluation metrics for computational costs: floating-point operations (FLOPs) and the number of parameters. FLOPs measure the number of floating-point operations required by the model during the inference process, while the number of parameters evaluates the model's size and storage requirements.



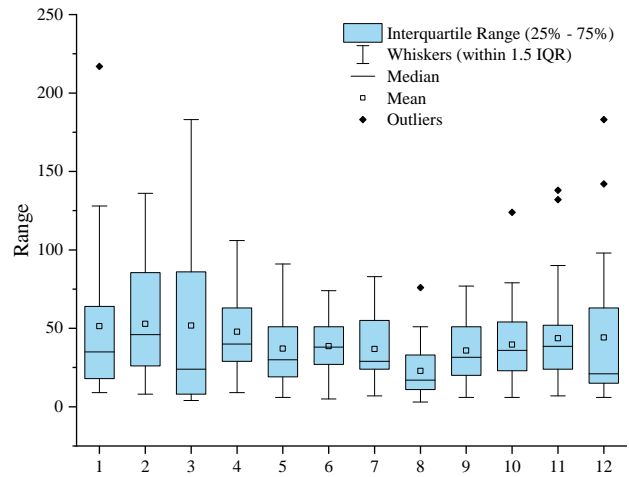
(a) Monthly distribution of air quality days in a specific region of Jiangsu Province, 2015



(b) Monthly distribution of air quality days in Beijing, 2019



(c) Monthly variation of PM2.5 concentrations in a specific region of Jiangsu Province, 2015



(d) Monthly variation of PM2.5 concentrations in Beijing, 2019

Fig. 4. Analysis of Air Quality and PM2.5 Concentrations in Jiangsu Province (2015) and Beijing (2019)

5.1.4. Computer environment

The experiments are conducted on two distinct setups. One includes a GeForce RTX 4090 GPU and a 13th Gen Intel(R) Core(TM) i9-13900KF processor on Ubuntu 22.04.3 LTS. Another includes a GeForce RTX 4060Ti GPU and a 13th Gen Intel(R) Core(TM) i5-13400F processor on Windows 11. Both configurations use Python 3.10 and the Pytorch deep learning framework.

5.2. Analysis of air quality

In this section, we analyze the air quality of a specific region in Jiangsu Province in 2015 and the air quality in Beijing in 2019. The air quality datasets for both locations can be found at <https://www.aqistudy.cn/historydata/>.

Fig. 4(a) and 4(b) show the monthly air quality days for a region in Jiangsu and Beijing, respectively. It can be observed that there are more days with severe pollution

in January and December, while the air quality is better in the summer. Fig. 4(c) and 4(d) present the monthly variation of PM2.5 concentrations in the same regions. PM2.5 concentrations fluctuate significantly in winter while they remain relatively stable in summer.

From the four figures, we can conclude that air quality in both datasets exhibits significant seasonal variations, with more severe pollution levels typically occurring during the winter months, particularly in January. The data shows that PM2.5 concentrations in January are highly variable, with a wide range of values and numerous outliers, indicating unstable and often high pollution levels.

Based on the above analysis, we selected the January data from the two datasets for single-step forecasting experiments. For multi-step forecasting experiments, we used the Beijing data from January to March, where the first 12 points were used to predict the subsequent 4 points.

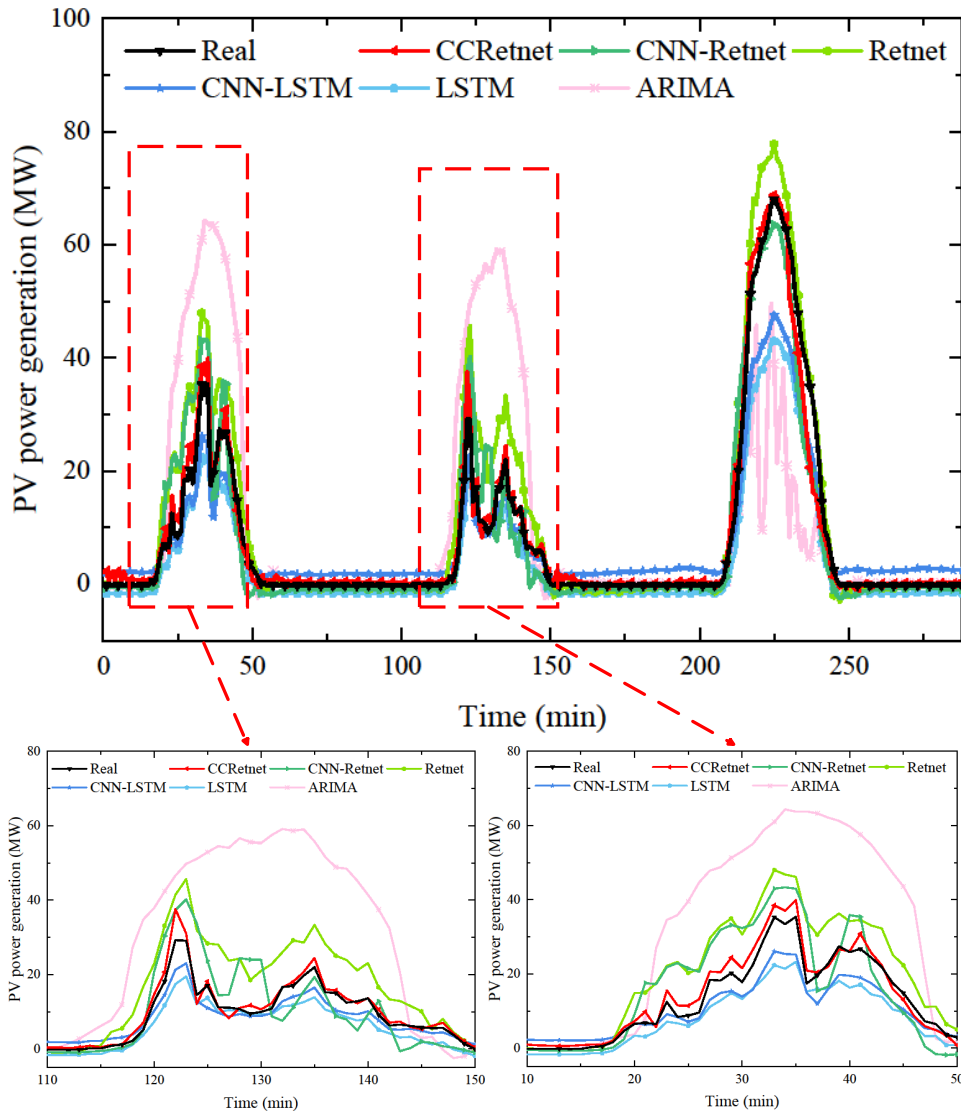
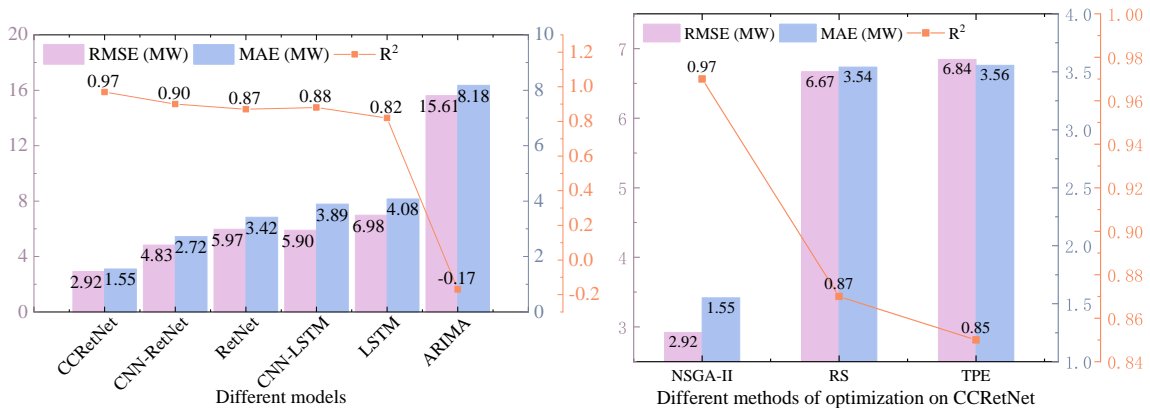


Fig. 5. Comparison of PV power generation forecasting on different models in a specific region of Jiangsu Province, January 2015



(a) Evaluation metrics of different models in a specific region of Jiangsu Province, January 2015
 (b) Evaluation metrics of different optimization methods on CCRetNet in a specific region of Jiangsu Province, January 2015

Fig. 6. Comparison of evaluation metrics and optimization methods for PV power generation forecasting in Jiangsu Province, January 2015

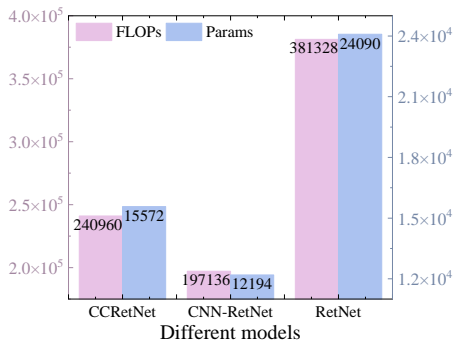


Fig. 7. The computational costs on different models in a specific region of Jiangsu Province, January 2015

5.3. Experimental results and analysis

We conduct experiments using two datasets, with the results discussed in Section 5.3.1, Section 5.3.2, and Section 5.3.3.

We compare the proposed model with eight traditional models, including CCRetNet, CNN-Retnet, Retnet, CNN-LSTM, CNN-GRU, CNN-RNN, long short term memory (LSTM), gate recurrent unit (GRU), recurrent neural network (RNN), autoregressive integrated moving average model (ARIMA) and Transformer. We utilize the Optuna library for hyperparameters and choose three methods for comparison: NSGA-II, random search (RS), and tree-structured parzen estimator (TPE). Model performance is evaluated based on accuracy and computational costs.

5.3.1. Analysis of single-step forecasting experiments in Jiangsu Province, 2015

In this section, we emphasize the experimental outcomes of multiple forecasting models applied to a specific region of Jiangsu Province dataset.

We compare the forecasting performance of various models, highlighting the superiority of CCRetNet in handling significantly fluctuating real data. Fig. 5 presents the forecasting results, while Fig. 6(a) provides numerical analysis. CCRetNet performs best when real data fluctuates considerably, with the lowest RMSE and MAE values of 2.71 MW and 2.55 MW and R^2 value of 0.97, higher than the other models, demonstrating its superiority. In contrast, ARIMA performs poorly when real data fluctuates significantly, with a negative R^2 value, indicating that it is unsuitable for PV forecasting on this dataset, especially during hazy weather.

The ablation experiments further verify the superiority of CCRetNet. Fig. 5 and Fig. 6(a) show that CCRetNet outperforms CNN-RetNet, primarily due to the clustering method based on TEWPP, which effectively qualifies uncertainty during hazy weather and classifies them within the clustering module. Fig. 5 and Fig. 6(a) also indicate that CNN-RetNet performs better than RetNet due to the introduction of CNN. The effectiveness of CNN is further supported by comparisons with other CNN-based deep learning models and general deep learning models.

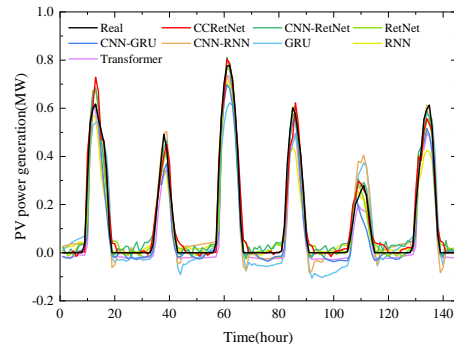


Fig. 8. Comparison of PV power generation forecasting on different models in Beijing, January 2019

Fig. 6(b) shows the accuracy of CCRetNet under different optimization methods across three evaluation metrics. The model optimized by NSGA-II outperforms the others. The model optimized by RS also shows commendable performance with a robust R^2 value, suggesting a reliable predictive capability. The model optimized by TPE appears less effective, as it exhibits the highest RMSE and MAE of others.

Fig. 7 illustrates the computational costs of the three models. RetNet incurs the highest computational costs. Although CCRetNet's computational costs are slightly higher than that of CNN-RetNet, the introduction of hierarchical clustering significantly improves CCRetNet's forecasting accuracy and trend performance.

5.3.2. Analysis of single-step forecasting experiments in Beijing, 2019

This section presents the performance analysis of various forecasting models on the Beijing dataset, highlighting both trend alignment and numerical accuracy.

Fig. 8 compares the actual values and the forecasts of traditional models on the Beijing dataset for January 2019. Overall, the R^2 values indicate that traditional models perform better on the Beijing dataset than on the Jiangsu dataset. CCRetNet exhibits minimal deviation from actual results during stable periods, although its performance during peak values is comparable to other traditional models as shown in Fig. 8.

Moreover, Fig. 10(a) reveals that CCRetNet achieves the smallest deviation from actual results, with the ablation experiment further confirming its superiority over CNN-RetNet, particularly due to the effectiveness of TEWPP-based clustering in qualifying uncertainty.

Fig. 10(c) compares the performance of CCRetNet under different optimization methods. The model optimized by NSGA-II achieves the best forecasting accuracy, evidenced by the lowest RMSE and MAE. The models optimized by TPE and RS both outperform the NSGA-II optimized model. However, they show similar forecasting accuracy on the Beijing dataset, which differs from the results on the Jiangsu dataset.

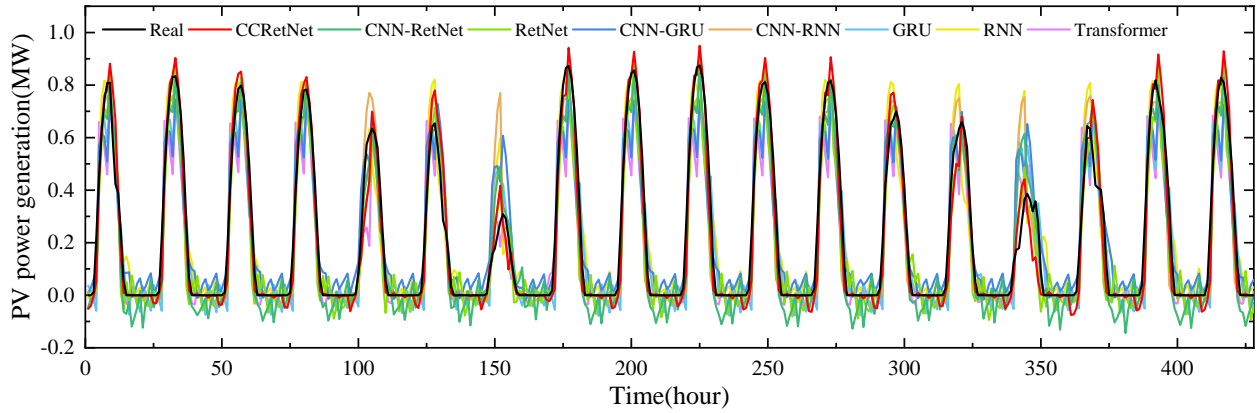
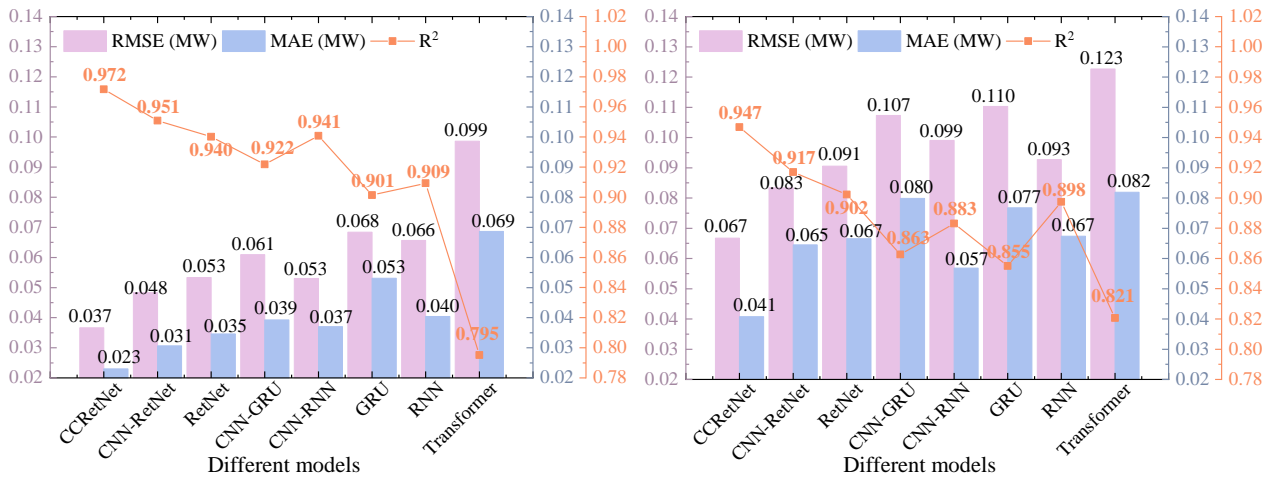
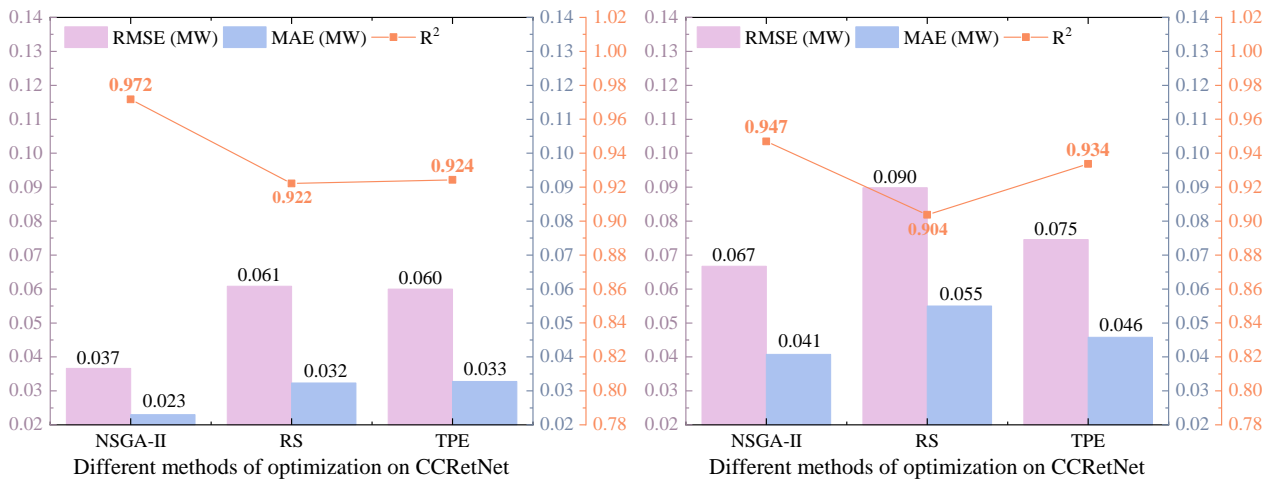


Fig. 9. Comparison of PV power generation forecasting on different models in Beijing, March 2019



(a) Evaluation metrics of different models in Beijing, January 2019

(b) Evaluation metrics of different models in Beijing, March 2019



(c) Evaluation metrics of different optimization methods on CCRetNet in Beijing, January 2019

(d) Evaluation metrics of different optimization methods on CCRetNet in Beijing, March 2019

Fig. 10. Comparison of evaluation metrics and optimization methods for PV power generation forecasting in Beijing, January and March 2019

5.3.3. Analysis of multi-step forecasting experiments in Beijing, 2019

In this section, we present the experimental results of several multi-step forecasting models on the Beijing dataset.

In multi-step forecasting experiments, most models perform worse than in single-step forecasting, as shown in Fig. 9, Fig. 10(b), and Fig. 10(d). Although the MSE and MAE of CNN-BiLSTM and Transformer are higher in multi-step forecasting, the R^2 is closer to 1 compared to single-step forecasting.

In the ablation experiments, CCRetNet exhibits smaller forecasting fluctuations compared to other models when PV power generation is stable, similar to the results of single-step forecasting. The ablation experiments also demonstrate the superiority of the clustering method based on TEWPP and CNN method.

The CCRetNet model optimized by NSGA-II performs the best in multi-step forecasting, comparing optimization methods. As shown in Fig. 10(d), the model optimized by TPE shows better forecasting accuracy than the model optimized by RS. However, both are outperformed by the model optimized by NSGA-II, a result that contrasts with the previous two experiments.

6. Conclusion

This study focuses on qualifying uncertainty in a series of PV power generation during hazy weather. The effectiveness of the proposed model is validated with two datasets. We create TEWPP to qualify uncertainty during hazy weather. Additionally, we use a novel median linkage method for hierarchical clustering to reduce computational costs. The optimal number of clusters k is determined using the silhouette coefficient. Multiple CCRetNet models are trained and tested for various categories and hyperparameters optimized by the NSGA-II algorithm. The results indicate that CCRetNet outperforms other comparative models regarding RMSE, MAE, and R^2 for short-term forecasting.

The study focuses on PV forecasting during hazy weather without considering other weather scenarios. Therefore, our future research aims to create a more efficient and adaptable framework by focusing on year-round weather conditions to make forecasts better.

CRedit authorship contribution statement

Xuan Yang: Conceptualization, Methodology, Data curation, Software, Writing - Original draft preparation. **Yunxuan Dong:** Data curation, Writing - Original draft preparation. **Lina Yang:** Supervision, Writing - review & editing. **Thomas Wu:** Supervision, Writing - review & editing.

References

[1] Z. Song, S. Cao, H. Yang, Quantifying the air pollution impacts on solar photovoltaic capacity factors and potential benefits of pollution control for the solar sector in china, *Appl. Energy* 365 (2024) 123261.

[2] M. Yu, D. Niu, K. Wang, R. Du, X. Yu, L. Sun, F. Wang, Short-term photovoltaic power point-interval forecasting based on double-layer decomposition and WOA-BiLSTM-Attention and considering weather classification, *Energy* 275 (2023) 127348.

[3] International Renewable Energy Agency (IRENA), Renewable Capacity Statistics 2024, <https://www.irena.org/>, 2024.

[4] M. Zhang, Y. Han, C. Wang, P. Yang, C. Wang, A.S. Zalhaf, Ultra-short-term photovoltaic power prediction based on similar day clustering and temporal convolutional network with bidirectional long short-term memory model: A case study using dkasc data, *Appl. Energy* 375 (2024) 124085.

[5] Y. Udagawa, K. Ogimoto, J.G. da Silva, F. Junior, H. Ohtake, S. Fukutome, Economic impact of photovoltaic power forecast error on power system operation in Japan, in: *IEEE Manch. PowerTech*, IEEE, pp. 1–6.

[6] O. Gandhi, W. Zhang, D.S. Kumar, C.D. Rodríguez-Gallegos, G.M. Yagli, D. Yang, T. Reindl, D. Srinivasan, The value of solar forecasts and the cost of their errors: A review, *Renew. Sust. Energ. Rev.* 189 (2024) 113915.

[7] T.N. Nguyen, F. Müsgens, What drives the accuracy of PV output forecasts?, *Appl. Energy* 323 (2022) 119603.

[8] S.A. Sadat, B. Hoex, J.M. Pearce, A review of the effects of haze on solar photovoltaic performance, *Renew. Sust. Energ. Rev.* 167 (2022) 112796.

[9] C. Zhang, C. Shen, Q. Yang, S. Wei, G. Lv, C. Sun, An investigation on the attenuation effect of air pollution on regional solar radiation, *Renew. Energy* 161 (2020) 570–578.

[10] B. Guo, Y. Wang, X. Zhang, H. Che, J. Zhong, Y. Chu, L. Cheng, Temporal and spatial variations of haze and fog and the characteristics of PM_{2.5} during heavy pollution episodes in china from 2013 to 2018, *Atmos. Pollut. Res.* 11 (2020) 1847–1856.

[11] M. Ma, B. He, Q. Lv, R. Shen, H. Zhu, R. Hou, A new power forecasting method for photovoltaic plants under hazy conditions, in: *2021 13th IEEE PES Asia Pacific Power & Energy Engineering Conference (APPEEC)*, IEEE, pp. 1–6.

[12] G. Jumarie, Derivation of an amplitude of information in the setting of a new family of fractional entropies, *Inf. Sci.* 216 (2012) 113–137.

[13] C. Yu, J. Qiao, C. Chen, C. Yu, X. Mi, TFEformer: A new temporal frequency ensemble transformer for day-ahead photovoltaic power prediction, *J. Clean Prod.* (2024) 141690.

[14] X. Zhou, Y. Ao, X. Wang, X. Guo, W. Dai, Learning with privileged information for short-term photovoltaic power forecasting using stochastic configuration network, *Inf. Sci.* 619 (2023) 834–848.

[15] Y. Niu, J. Wang, Z. Zhang, T. Luo, J. Liu, De-trend first, attend next: A mid-term PV forecasting system with attention mechanism and encoder–decoder structure, *Appl. Energy* 353 (2024) 122169.

[16] L. Zhang, J. Zhu, D. Zhang, Y. Liu, An incremental photovoltaic power prediction method considering concept drift and privacy protection, *Appl. Energy* 351 (2023) 121919.

[17] D. Jia, L. Yang, T. Lv, W. Liu, X. Gao, J. Zhou, Evaluation of machine learning models for predicting daily global and diffuse solar radiation under different weather/pollution conditions, *Renew. Energy* 187 (2022) 896–906.

[18] W. Yao, C. Zhang, H. Hao, X. Wang, X. Li, A support vector machine approach to estimate global solar radiation with the influence of fog and haze, *Renew. Energy* 128 (2018) 155–162.

[19] J. Fan, L. Wu, F. Zhang, H. Cai, X. Wang, X. Lu, Y. Xiang, Evaluating the effect of air pollution on global and diffuse solar radiation prediction using support vector machine modeling based on sunshine duration and air temperature, *Renew. Sust. Energ. Rev.* 94 (2018) 732–747.

[20] W. Yao, C. Zhang, X. Wang, J. Sheng, Y. Zhu, S. Zhang, The research of new daily diffuse solar radiation models modified by air quality index (AQI) in the region with heavy fog and haze, *Energy Conv. Manag.* 139 (2017) 140–150.

[21] J. Qu, Z. Qian, Y. Pei, Day-ahead hourly photovoltaic power forecasting using attention-based CNN-LSTM neural network embedded with multiple relevant and target variables prediction pattern, *Energy*

- 232 (2021) 120996.
- [22] M. Wang, C. Rao, X. Xiao, Z. Hu, M. Goh, Efficient shrinkage temporal convolutional network model for photovoltaic power prediction, *Energy* (2024) 131295.
- [23] J. Fan, L. Wu, X. Ma, H. Zhou, F. Zhang, Hybrid support vector machines with heuristic algorithms for prediction of daily diffuse solar radiation in air-polluted regions, *Renew. Energy* 145 (2020) 2034–2045.
- [24] Z. Zhang, J. Wang, D. Wei, Y. Xia, An improved temporal convolutional network with attention mechanism for photovoltaic generation forecasting, *Eng. Appl. Artif. Intell.* 123 (2023) 106273.
- [25] A. Rai, A. Shrivastava, K.C. Jana, Differential attention net: Multi-directed differential attention based hybrid deep learning model for solar power forecasting, *Energy* 263 (2023) 125746.
- [26] C. Huang, M. Yang, Memory long and short term time series network for ultra-short-term photovoltaic power forecasting, *Energy* (2023) 127961.
- [27] H. He, Q. Zhang, S. Bai, K. Yi, Z. Niu, CATN: Cross attentive tree-aware network for multivariate time series forecasting, in: *Proceedings of the AAAI Conference on Artificial Intelligence*, volume 36, pp. 4030–4038.
- [28] D. Shang, P. Shang, A. Li, A novel clustering method for complex signals and feature extraction based on advanced information-based dissimilarity measure, *Expert Syst. Appl.* 238 (2024) 122011.
- [29] B. Fadlallah, B. Chen, A. Keil, J. Principe, Weighted-permutation entropy: A complexity measure for time series incorporating amplitude information, *Phys. Rev. E* 87 (2013) 022911.
- [30] G. Qin, P. Shang, Analysis of time series using a new entropy plane based on past entropy, *Chaos Solitons Fractals* 152 (2021) 111477.
- [31] P.J. Rousseeuw, Silhouettes: a graphical aid to the interpretation and validation of cluster analysis, *J. Comput. Appl. Math.* 20 (1987) 53–65.
- [32] Y. Sun, L. Dong, S. Huang, S. Ma, Y. Xia, J. Xue, J. Wang, F. Wei, Retentive network: A successor to transformer for large language models, *arXiv preprint arXiv:2307.08621* (2023).
- [33] S. Islam, H. Elmekki, A. Elsebai, J. Bentahar, N. Drawel, G. Rjoub, W. Pedrycz, A comprehensive survey on applications of transformers for deep learning tasks, *Expert Syst. Appl.* (2023) 122666.

Appendix

An example of weather data is as follows:

Table 1: Air quality data in the specific Jiangsu region, January 2015

date	AQI	Quality Level	PM2.5	PM10	SO2	NO2	CO	O3	Hazy weather
2015/1/1	79	Good	54	107	42	19	1	76	No
2015/1/2	114	Mild Pollution	86	142	60	31	1.4	64	Yes
2015/1/3	148	Mild Pollution	114	161	58	41	1.5	59	Yes
2015/1/4	217	Severe Pollution	167	230	61	50	1.6	86	Yes
2015/1/5	228	Severe Pollution	178	218	38	42	1.6	48	Yes
2015/1/6	68	Good	44	86	24	7	0.8	85	No
2015/1/7	75	Good	50	100	45	20	1	75	No
2015/1/8	129	Mild Pollution	98	133	54	33	1.4	78	Yes
2015/1/9	220	Severe Pollution	170	220	63	53	1.7	107	Yes
2015/1/10	280	Severe Pollution	230	299	67	54	2	117	Yes
2015/1/11	164	Moderate Pollution	125	188	52	33	1.3	83	Yes
2015/1/12	41	Excellent	18	41	16	12	0.6	81	No
2015/1/13	40	Excellent	15	36	12	16	0.5	79	No
2015/1/14	34	Excellent	24	27	14	13	0.5	68	No
2015/1/15	124	Mild Pollution	94	125	34	32	1.2	59	Yes
2015/1/16	192	Moderate Pollution	145	173	36	32	1.3	67	Yes
2015/1/17	78	Good	56	107	20	13	0.9	121	No
2015/1/18	73	Good	54	90	32	27	1	68	No
2015/1/19	144	Mild Pollution	66	178	37	22	0.9	67	Yes
2015/1/20	59	Good	24	68	16	15	0.7	79	No
2015/1/21	105	Mild Pollution	79	111	24	29	1.2	57	Yes
2015/1/22	101	Mild Pollution	76	103	22	19	1.1	46	Yes
2015/1/23	168	Severe Pollution	127	173	32	37	1.5	68	Yes
2015/1/24	103	Mild Pollution	77	103	19	28	1	90	Yes
2015/1/25	122	Mild Pollution	92	120	15	24	1.1	69	Yes
2015/1/26	147	Mild Pollution	112	142	25	17	1.3	74	Yes
2015/1/27	58	Good	37	65	16	8	0.8	79	No
2015/1/28	41	Excellent	14	36	12	7	0.5	82	No
2015/1/29	48	Excellent	34	45	12	11	0.7	76	No
2015/1/30	100	Good	75	113	34	22	1.2	77	No
2015/1/31	50	Excellent	22	50	17	10	0.8	86	No